Quasi-static crack propagation in plane and plate structures using set-valued traction-separation laws

Pedro M. A. Areias[1,*,†] and Timon Rabczuk[2]

[1]*Computational Science and Engineering, University of Illinois at Urbana-Champaign, 2233 Digital Computer Laboratory, MC-278, 1304 West Springfield Avenue, Urbana, IL 61801, U.S.A.*
[2]*Department of Mechanical Engineering, University of Canterbury, Christchurch 8140, New Zealand*

SUMMARY

We introduce a numerical technique to model set-valued traction-separation laws in plate bending and also plane crack propagation problems. By using of recent developments in thin (Kirchhoff–Love) shell models and the extended finite element method, a complete and accurate algorithm for the cohesive law is presented and is used to determine the crack path. The cohesive law includes softening and unloading to origin, adhesion and contact. Pure debonding and contact are obtained as particular (degenerate) cases. A smooth root-finding algorithm (based on the trust-region method) is adopted. A step-driven algorithm is described with a smoothed law which can be made arbitrarily close to the exact non-smooth law. In the examples shown the results were found to be step-size insensitive and accurate. In addition, the method provides the crack advance law, extracted from the cohesive law and the absence of stress singularity at the tip. Copyright © 2007 John Wiley & Sons, Ltd.

1. INTRODUCTION

Cohesive models of fracture are accepted as representative of the near-tip non-linear zone of quasi-brittle and certain ductile materials. The idea is attributed to Barenblatt [1]. These models have certain attractive properties; for example, a pre-existent crack is not necessary. Neither is the stress singularity in the crack tip, which requires a specific discretization to be represented. Because of this, numerous applications were carried out by several authors (reviews are available in [2–5]) and some software packages can currently be used. However, it is known that for the problem

---

*Correspondence to: Pedro M. A. Areias, Computational Science and Engineering, University of Illinois at Urbana-Champaign, 2233 Digital Computer Laboratory, MC-278, 1304 West Springfield Avenue, Urbana, IL 61801, U.S.A.
†E-mail: pareias@uiuc.edu

to be well posed, cohesive models must include an initially rigid behavior (or at least as stiff as possible, as indicated by Alfano and Crisfield [6]). In finite element codes, initially rigid models (also called extrinsic, see [7]) cannot be implemented when only displacement degrees of freedom are used, and regularization adversely affects the results [7, 8]. In particular, the crack profile and the cohesive zone length result are different.

For explicit codes, Papoulia *et al.* [9] and Sam *et al.* [8] proposed specialized time-step solutions, but the results can suffer from interpenetration stress locking due to opposite signs in stress and opening displacement (as indicated by the conclusions of Papoulia *et al.* [9]) and a new model was said to be required. At least two algorithms of solution to deal with the initially rigid behavior exist: event-driven and step-driven algorithms. A generic comparison between these methods is provided by Leine and Nijmeijer [10]. In summary, event-driven algorithms are analogous to constraint active-set strategies in optimization problems whereas step-driven methods use the state of the constraints at each pre-established time step. Step-driven methods are appropriate for problems with a large number of complementarity conditions, but are usually less accurate in terms of resolution [10]. We make use of a fixed-step-driven method and a smooth root finder.

The locking effect did not occur in the examples shown here. If we identify the problem as a non-linear complementarity problem (NCP see also [11], adhesion and unloading share the same law *unrelated* with the behavior of the adjacent continuum. We can therefore employ a rigorous surface-based traction-separation law with any particular continuum problem, regardless of the method used to obtain the stress in the continuum. The advantages of this approach were pointed out by T. Belytschko to the authors of this paper [12].

This differs from some perspectives in this field, where a continuum-based cohesive law (the continuum constitutive law has to correctly represent the pre-localization response, the localization surface and, in addition, the post-localization response) is often proposed. In the work of Huespe *et al.* [13], the authors claim that no discontinuities occur with the classical approach, but a comparison was not provided there. Here, we perform tests where interpenetration stress locking is absent. The stress state can travel in a vertical half-line limited by the maximum stress.

Analytical and numerical studies of fracture in plain strain and thin plates (plane stress) have been disseminated in the literature (see e.g. [14, 15]). These fail to provide a comprehensive solution to the traction-separation behavior.

The introduction of set-valued traction-separation laws in the discrete non-linear problem of cohesive fracture leads to an NCP that can be solved by B-smooth solvers [16], interior point methods or smoothing techniques [17]. The traction-separation laws contain an infinite initial stiffness and also a compliance in loading which varies with time as an internal variable evolves (note that, according to Elices *et al.* [4], hardening should be absent). Smoothing methods can be implemented and the Newton method can be made use of for smooth functions if some modifications are introduced in the discrete formulation.

We shall see that if these are done, both smooth and non-smooth problems can be solved with the same framework. From a solution viewpoint, either line search or trust-region methods can be used in the inner stage of the method; a continuation method with adaptive smoothing parameters was proposed by Chen and Harker [18].

Trust-region methods are appropriate for continuous but not necessarily 'quadratic-like' functions: the search direction is obtained as a convex combination of Newton and the steepest descent Cauchy step. A quadratic merit function is the indicator for the coefficient of the combination.

Caution is exerted in the formulation of the modified cohesive problem, as smoothing can introduce artificial spikes in the cohesive law. Details about this are given in Section 3. In addition,

only quasi-static growth is shown in this paper and the crack propagation is known to be stable for the experimental beam tests shown.

This paper is organized as follows: In Section 2 the relevant quantities and the formulation are introduced; in Section 3 the mixed method is discussed with a bi-linear cohesive law. Section 4 describes the crack advance condition, which is based on the tip force. Both 2D and plate bending examples are presented in Section 5. Finally, the conclusion follows in Section 6.

2. FORMULATION AND DISCRETIZATION

The constrained quasi-static thin plate bending problem consists of the equilibrium equation, mass conservation principle, the Kirchhoff–Love constraint, Dirichlet and Neumann boundary conditions, the stress–displacement jump cohesive law and the Cauchy lemma for the cohesive surface. These are grouped in the equation system (1). Figure 1 depicts the relevant ingredients. A 2D plane stress (or strain) problem can be solved with the same underlying theory by prescribing the out-of-plane displacement and modifying the elastic law.

The relevant domains are the body in deformed Ω and reference Ω_0 configurations, the crack core in the deformed Γ_c and reference Γ_{c0} configurations, the Dirichlet boundary $\Gamma_{\overline{u}}$ and Neumann boundary $\Gamma_{\overline{t}}$.

$$
\left.
\begin{aligned}
\mathrm{Div}\,\mathbf{P}^{\mathrm{T}} + \mathbf{b}_0 &= 0 \\
\rho_0 &= \det[\mathbf{F}]\rho \\
C_{i3} &= \delta_{i3}
\end{aligned}
\right\} \quad \text{for } \mathbf{x} \in \Omega
$$

$$
\mathbf{u} = \overline{\mathbf{u}} \quad \text{for } \mathbf{x} \in \Gamma_{\overline{u}} \tag{1}
$$

$$
\mathbf{t} = \overline{\mathbf{t}} \quad \text{for } \mathbf{x} \in \Gamma_{\overline{t}}
$$

$$
\mathrm{eq}\,(\sigma_n, \Delta u) = 0 \quad \text{for } \mathbf{x} \in \Gamma_c
$$

$$
\det[\mathbf{F}]\sigma_n = \mathbf{n}_c^{\mathrm{T}}(\mathbf{P}\mathbf{N}_c) \quad \text{for } \mathbf{x} \in \Gamma_c
$$

In (1), $\mathbf{P}$ is the first Piola–Kirchhoff stress tensor and $\mathbf{b}_0$ is the volume force vector in the reference configuration; ρ_0 and ρ are the reference and deformed mass density, respectively. The customary notation is employed for the coordinates of a given point X: $\mathbf{X}$ is the reference position vector and $\mathbf{x}$ is the deformed reference position vector. The deformation gradient, $\mathbf{F}$, is given by $\partial\mathbf{x}/\partial\mathbf{X}$. The deformed and reference cohesive surface normals are related by

$$
\mathbf{N}_c = \left(\frac{\partial\mathbf{x}}{\partial\mathbf{X}}\right)^{\mathrm{T}}\mathbf{n}_c \tag{2}
$$

Note that (2) could also be written, in a more traditional form, with the use of norms.

The outer boundary of Ω, $\partial\Omega$ is partitioned into two boundaries: $\partial\Omega = \Gamma_{\overline{u}} \cup \Gamma_{\overline{t}}$. For a plate or shell, mid-surface coordinates θ^1 and θ^2 and a signed distance to the mid-surface θ^3 are introduced so that an appropriate form of the equilibrium equation is obtained, based on one-to-one correspondence $\mathbf{X} \leftrightarrow \theta^i$. For convenience, the mid-surface coordinates θ^1 and θ^2 are indexed as α and β (see [19]). Derivatives of a quantity $(\bullet)$ with respect to α are represented as $(\bullet)_{,\alpha}$.
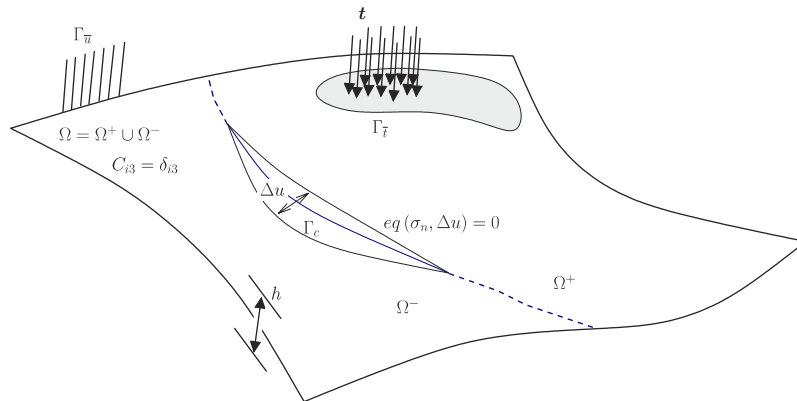
Figure 1. Relevant quantities of the cohesive problem. The equation $\text{eq}(\sigma_n, \Delta u) = 0$ represents the force-displacement constraint corresponding to a particular traction-separation model. The thickness h is assumed to be uniform.

Using this nomenclature, the weak form of the equilibrium equation is

$$\int_\Omega s^{\alpha\beta} \mathbf{x}_{,\beta} \cdot \delta\mathbf{x}_{,\alpha} \sqrt{G} \, \mathrm{d}\theta^1 \, \mathrm{d}\theta^2 \, \mathrm{d}\theta^3 = \delta W_E \tag{3}$$

where $s^{\alpha\beta}$ are scalar components of the second Piola–Kirchhoff stress in the basis $\mathbf{X}_\alpha \otimes \mathbf{X}_\beta$ with $\alpha = 1, 2$ and $\beta = 1, 2$. The Jacobian determinant is defined as $\sqrt{G} = \mathbf{X}_{,1} \cdot (\mathbf{X}_{,2} \times \mathbf{X}_{,3})$.

Recently, in [15], we introduced a method based on overlapping paired elements (applied to 4-node quadrilaterals) to represent crack propagation in thin shells that allows a relatively direct implementation of element-wise fracture in plates and shells. The method uses two distinct deformation maps, one for each part of the cracked shell. In pristine regions, the deformation maps coincide. A signed distance function $g(\mathbf{X})$ is adopted to identify the crack core Γ_c.

In the discretization by finite elements, the degrees of freedom are mid-side rotations and corner-node displacements. Local duplication of homologous degrees of freedom is used in cracked elements. The basis functions agree with those of the extended finite element method (XFEM) (e.g. [20–22]), but a different perspective is adopted. Additionally, in the present context, four additional degrees of freedom per element are used corresponding to the cohesive stresses.

Note that the directors in the deformed configuration follow independent deformation maps. Using the signed distance to the crack surface, $g(\mathbf{X})$ such that $g(\mathbf{X}) < 0$ for $\mathbf{X} \in \Omega^-$, $g(\mathbf{X}) > 0$ for $\mathbf{X} \in \Omega^+$ and $\mathbf{X} = 0$ for $\mathbf{X} \in \Gamma_{c0}$ we have $\Gamma_{c0} = \{\mathbf{X}_c \in \mathbb{R}^3 : g(\mathbf{X}_c) = 0\}$.

The shell element used in the discretization contains four corner nodes where the mid-surface positions are interpolated and four mid-sides where rotations are interpolated. Implementation details are given in Reference [15]. For completeness, we provide the deformation map (in Ω):

$$\mathbf{x} \equiv \boldsymbol{\varphi}(\mathbf{X}) = \begin{cases} \underbrace{\mathbf{r}^+(\boldsymbol{\theta}) + \theta^3 \mathbf{n}^+(\boldsymbol{\theta})}_{\mathbf{x}^+}, & g(\mathbf{X}) > 0 \\ \underbrace{\mathbf{r}^-(\boldsymbol{\theta}) + \theta^3 \mathbf{n}^-(\boldsymbol{\theta})}_{\mathbf{x}^-}, & g(\mathbf{X}) < 0 \end{cases} \tag{4}$$

where $\mathbf{r}$ is the mid-surface position and $\mathbf{n}$ the deformed director field.

The Cauchy Lemma and the cohesive law use specific quadrature points of the XFEM. The tip advance criterion is the internal force at the tip.

3. NON-SMOOTH COHESIVE LAW AND THE MIXED METHOD

3.1. Introduction to cohesive traction-separation laws

The concept of cohesive force by Barenblatt [23, 24] (a review is presented in Reference [1]) implies the finiteness of the stress caused by canceling of the singularity in the Westergaard asymptotic field with the singularity created by a cohesive tip. A depiction of this concept is provided in Figure 2, where the mobile equilibrium crack (see Barenblatt [1] and Goodier [25]) is represented. The position of points A and B is obtained as part of the solution of the constrained boundary-value problem (BVP) stated in (1). The fracture process zone (FPZ) is associated with a fracture stress $f(x, d)$, where x is the position along the crack and d is the opening at a given position. Point A, which is the infimum in x of the support of the cohesive force function $f(x, d)$, is a function of the opening displacement. Point B is distinct: its motion is a consequence of equilibrium (hence the name equilibrium crack) by the imposition of a null stress intensity factor. Other conditions are equivalent to this one: the maximum stress ahead of the tip or the cusp-type shape of the opening profile of a cohesive crack. A zero force to close the tip is also an equivalent in the discrete setting.

We direct the reader to the textbook by Bažant and Planas [3] for a description and to the paper by Moës and Belytschko [26] for an application of this concept with the XFEM. It is worth noting that cohesive laws are subject to the condition that contact complementarity should be obtained as a limit case (null fracture energy and maximum stress). Smoothing of the contact linear complementarity problem (LCP) has been performed by Eterovic and Bathe [27].

The numerical treatment of cohesive laws appears to be less studied than the applications. Originally, regularization was employed in the loading/unloading region of the curves and often intrinsic (and in certain cases holonomic, see [26]) laws were employed in numerical applications. Smooth loading laws were used by Xu and Needleman [28] but do not constitute a solution for the implementation in a displacement-based context.

After the papers by Falk *et al.* [29] and Alfano and Crisfield [6], it became clearer that results of initially rigid laws are different from those obtained with regularization, namely in the multi-fracture and bifurcation contexts (see also [8]). Furthermore, very rigid laws induce greater condition
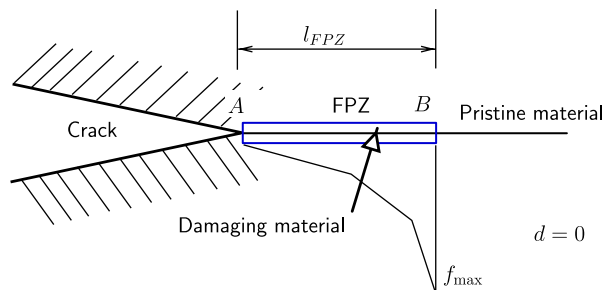

Figure 2. The mobile equilibrium crack (see [1, 25]) and the fracture process zone (FPZ): points A and B move according to the released energy and are denoted here as configurational points.
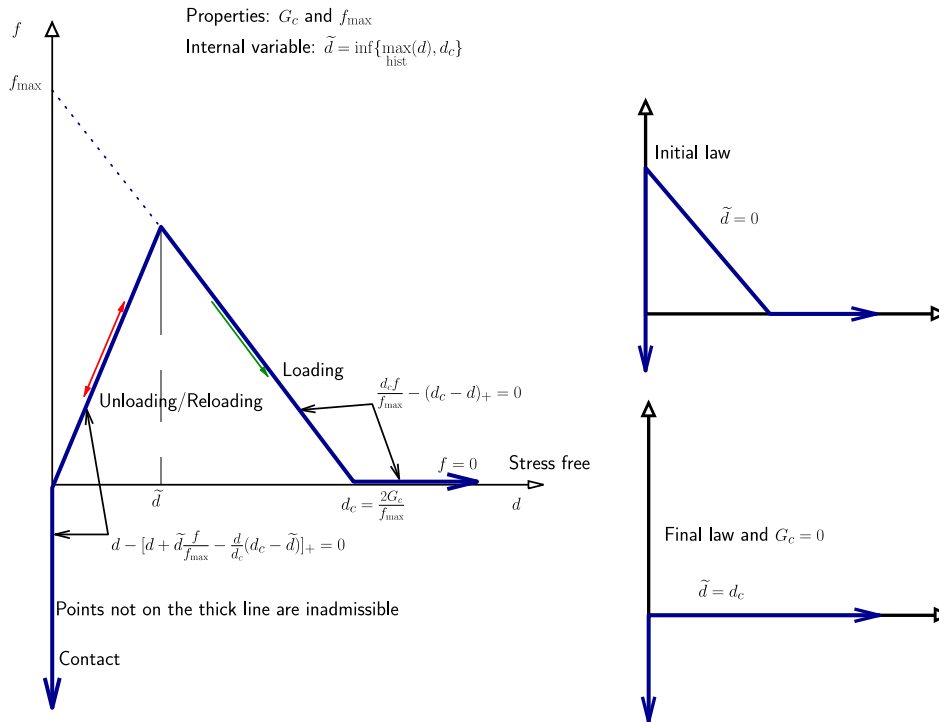
Figure 3. The prototype model for the cohesive law. Unloading occurs at the origin. At a given time step, the internal variable $\widetilde{d}$ is fixed. Two degenerate cases are shown: the initial law and the contact problem.

numbers of the Jacobian matrix in an implicit solution framework. The cohesive problem with unloading is non-holonomic, which means that the conditions can only be written with rate kinematical quantities (this also occurs with elasto-plasticity or when two rigid objects contact in rolling [30]).

The identification of this problem as a complementary problem appears to have been first done by Bolzon *et al.* [11] (a more complete analysis was performed by Tin-Loi and Tseng [31]). However, the implementations are not amenable to be incorporated in classical finite element codes. The authors in [31] have dealt exclusively with holonomic mode I, despite having a correct representation of the initial infinite slope. The authors in [11] used a rigid-plastic law, which resulted in a discrete variational inequality analogous to the one of elasto-plasticity and hence the same algorithms could be employed. More recently, Tin-Loi and Que [32] performed a comparison (limited to the holonomic case) between several methods to solve an LCP and concluded that smoothing methods are appropriate from both the accuracy and efficiency viewpoints. One striking fact in these tests is that no special treatment of the initial infinite slope was discussed, which is the most troublesome aspect in modeling cohesive laws. We try to avoid the simplifications in these works and will see that the complete non-holonomic treatment makes use of a separate inspection of two degenerate cases.
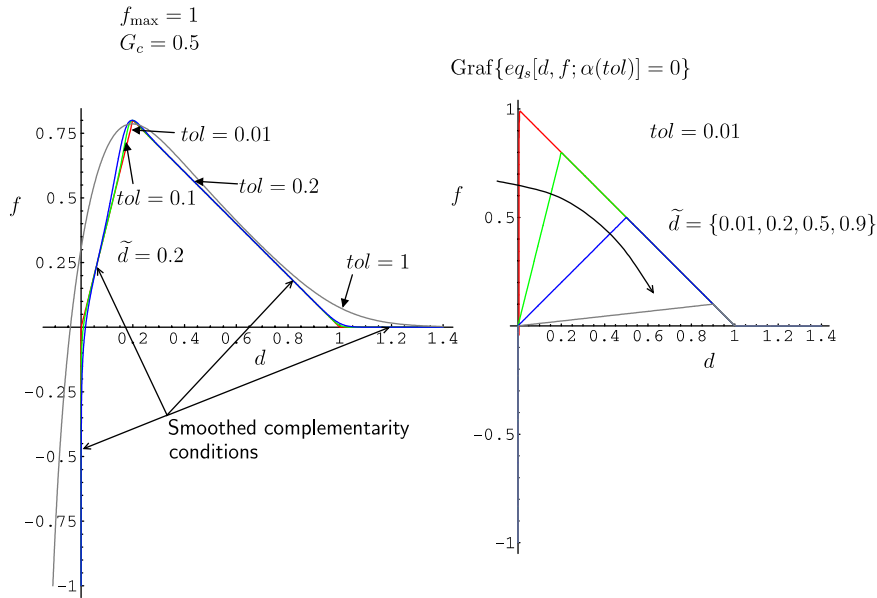
Figure 4. Smoothed cohesive laws for various tol and $\widetilde{d}$.

We review the typical initially rigid cohesive law as depicted in Figure 3. The area enclosed between the initial loading curve and the d-axis equals the critical fracture energy G_c, as deduced by use of the J integral (e.g. see [33, p. 167]). We note that two complementarity conditions exist for non-degenerate cases. For degenerate cases, only one complementarity condition exists. The contact/unloading/reloading curve is valid for $f < f_{\max}$ and $d \leqslant \widetilde{d}$ and the loading/stress free curve is valid for $d > \widetilde{d}$ or $f \geqslant f_{\max}$.

The existence of the two degenerate cases and a set-valued force inhibits the use of standard displacement-based methods. Note that the second degenerate case corresponds to the contact LCP and occurs with $\widetilde{d} = d_c$. It is also noteworthy that if $G_c = 0$, it follows that $d_c = 0$ and no characteristic length exists. However, a characteristic force exists ($f_{\max}$). In such a case, the drop $f_{\max} \to 0$ occurs instantaneously, with debonding of the cohesive surface. The switch condition between these two conditions is an added complication that has not, to the authors' knowledge, been treated before.

A method to solve this problem consists in smoothing both the complementarity conditions and the switch condition and performing the iteration in the force–displacement space. This increases the total number of degrees of freedom but results in a well-conditioned algebraic (non-symmetric) problem. We make use of a trust-region algorithm (see also [34]) to solve the constrained equilibrium problem.

3.2. Effect of smoothed functions

Replacement of the 'step' and 'plus' functions by smooth approximations allows the use of Newton-based root-finding algorithms. We view smoothing as distinct of regularization, as the latter results in additional stiffness in the algebraic system. The purpose of smoothing is the replacement of
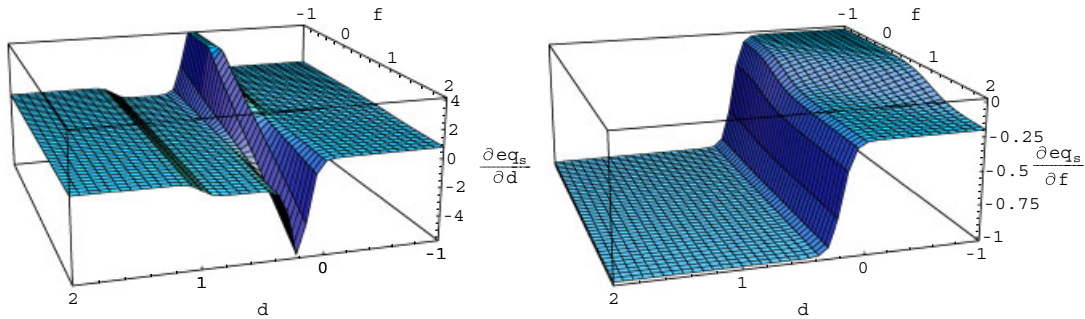
Figure 5. Smoothed cohesive laws: derivatives of the constraint $\mathrm{eq}_s(d, f) = 0$ with respect to d and f in the d–f space. tol$=0.5$ and $\tilde{d}=0.2$.

complementarity conditions and other non-smooth conditions (such as branches) by more tractable constraints in the force (or stress)–displacement space.

For the linear case a perturbed method was proposed by Chen and Harker [35] where the orthogonality condition was relaxed. With smoothing methods this condition is also relaxed. For the non-linear case, it was found by Chen and Mangasarian [17] that, under certain conditions, the smooth problem is solvable and has as limit the solution of the NCP.

We make use of part of the formulation established in [17] where a method is proposed to solve non-linear (and also mixed) complementarity problems. Instead of the line search used in their work, we use here a trust-region method because the crack opening modifies the radius of convergence of the Newton method, as will be shown.

Chen and Mangasarian [17] provide a catalog of smooth replacement functions. We direct the reader to the proofs by Chen and Harker [18] and Chen and Mangasarian [17]. In particular, as a relation is established with interior point methods, proofs concerning the iteration trajectory make use of similar conclusions.

A smooth modification of the step function is given by ($x \in \mathbb{R}$)

$$s(x, \alpha) = \frac{1}{1 + \mathrm{e}^{-\alpha x}} \tag{5}$$

where the parameter α can be calculated for a given tolerance. We prescribe tol$=x_{s=1-\varepsilon} - x_{s=\varepsilon}$ and obtain

$$\alpha = \frac{2}{\mathrm{tol}} \ln\left(\frac{1-\varepsilon}{\varepsilon}\right) \tag{6}$$

This smooth function can be derived using probability density functions. Further properties are provided in References [17, 18]. The corresponding smoothed 'plus' function is given by integration of s:

$$p(x, \alpha) = x + \frac{1}{\alpha} \ln(1 + \mathrm{e}^{-\alpha x}) \tag{7}$$

with $p[x, \alpha(\mathrm{tol})] \leqslant x_+ + \log(2)/\alpha(\mathrm{tol})$ where $x_+ = \max(0, x)$. Note that the form of functions (5) and (7) is adequate for $x > 0$ but should be modified for $x < 0$ to avoid floating point overflow. The selection of these functions is not irrelevant for the solution. Other methods can be generated using

Table I. Trust-region method.

Step	Tasks
Initialization	
Data	$\text{tol}_{\text{tr}},\ R_0$
Iteration counter and initial radius	$n_{\text{iter}}=0,\ R=R_0$
Function evaluation	
Store previous values for $n_{\text{iter}}>0$	$\check{\text{f}}_{\text{old}}=\check{\text{f}}$
	$\mathfrak{m}_{\text{old}}=\mathfrak{m}$
Evaluate the residual	$\mathbf{F}$
Objective	$\check{\text{f}}=0.5\mathbf{F}\cdot\mathbf{F}$
Jacobian of F	$\mathbf{J}=\frac{\partial\mathbf{F}}{\partial\mathbf{z}}$
Jacobian of $\check{\text{f}}$	$\mathbf{g}=\mathbf{J}^{\text{T}}\mathbf{F}$
Temporary value	$\mathbf{p}=\mathbf{Jg}$
Update of radius	
Calculate merit for $n_{\text{iter}}>0$	$\mathbf{r}_d=\mathbf{Jd},\ \mathfrak{m}=\check{\text{f}}+\mathbf{d}\cdot\mathbf{g}+0.5\mathbf{r}_d\cdot\mathbf{r}_d$
Calculate evolution ratio $n_{\text{iter}}>1$	$\rho=\frac{\check{\text{f}}_{\text{old}}-\check{\text{f}}}{\mathfrak{m}_{\text{old}}-\mathfrak{m}}$
Update the radius for $n_{\text{iter}}>1$	$\rho<0\rightarrow R=0.5R$
	$0<\rho\leqslant0.95\rightarrow R=[0.5+0.5(\rho/0.95)^2]R$
	$\rho>0.95\rightarrow R=[1.01+0.99\text{e}^{-(\rho-1)/(0.95-1)^2}]R$
Step determination	
Newton step	$\mathbf{d}^N=-\mathbf{J}^{-1}\mathbf{F}$
Verify Newton step	$\|\mathbf{d}^N\|\leqslant\text{tol}_{\text{tr}}\rightarrow$ declare success and exit
	$\|\mathbf{d}^N\|\leqslant R\rightarrow\mathbf{d}=\mathbf{d}^N$ go to update of unknowns
Unconstrained step (Cauchy)	$\mathbf{d}^u=-\left(\frac{\mathbf{g}\cdot\mathbf{g}}{\mathbf{p}\cdot\mathbf{p}}\right)\mathbf{g}$
Verify unconstrained step	$\|\mathbf{d}^u\|\geqslant R\rightarrow\mathbf{d}=-\frac{R}{\|\mathbf{g}\|}\mathbf{g}$ go to update of unknowns
Dogleg	Solve for $h\in[0,1]:a_1h^2+a_2h+a_3=0$
	with $a_1=\|\mathbf{d}^N-\mathbf{d}^u\|^2,\ a_2=\mathbf{d}^u\cdot(\mathbf{d}^N-\mathbf{d}^u),\ a_3=\|\mathbf{d}^u\|^2-R^2$
	$\mathbf{d}=\mathbf{d}^u+h(\mathbf{d}^N-\mathbf{d}^u)$
Update of unknowns	
Make temporary update	$\mathbf{z}\leftarrow\mathbf{z}+\mathbf{d}$
	$n_{\text{iter}}=n_{\text{iter}}+1$ \qquad go to function evaluation

Note: The degrees of freedom u_i and f_j are grouped in array $\mathbf{z}$.

distinct functions. For example, an interior point method is generated by selecting an interior point smoothing function:

$$p_{\text{ip}}(x,\alpha)=\frac{x+\sqrt{x^2+4/\alpha}}{2} \tag{8}$$

As alluded to before, caution should be taken while using smoothed functions to avoid 'spikes'. For example, for a branch function such as $y=x/c_1:x<c_1,\ y=(1-x)/(1-c_1):x\geqslant c_1$ with $x\in[0,1]$ and $c_1\in[0,1]$, the maximum of y in this interval is 1; however, the corresponding smoothed function $y_s=p(c_1-x)x/c_1+p(x-c_1)(1-x)/(1-c_1)$ is unbounded as $c_1\rightarrow0$.
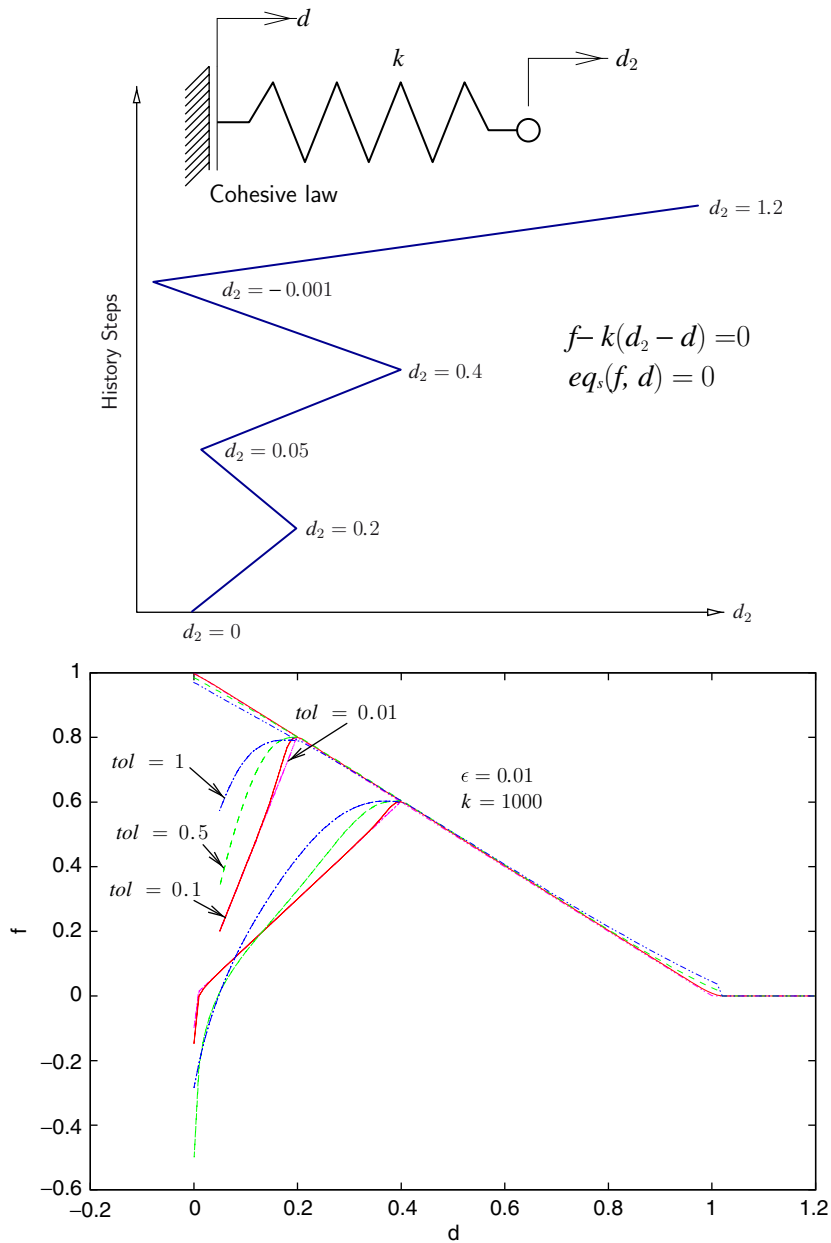
Figure 6. Effect of tol for a spring with an end cohesive law.

The smooth replacements must also ensure that the solution of the original problem is the same as the solution of the replacement problem as tol → 0. It is clear that $x_+ = \lim_{\alpha \to +\infty} p[x, \alpha]$. However, this should occur with the solution of the NCP problem, if it exists. Chen and Mangasarian [17]

Table II. Average number of iterations and maximum number
of iterations in a given time step, as a function of tol and n_{step}.

n_{step}	tol	$n_{\text{iter}}^{\text{av}}$	$n_{\text{iter}}^{\text{max}}$
300 steps	0.02	1.55	7
	0.05	1.72	9
	0.1	1.97	8
	0.5	2.10	6
	1	2.06	3
	2	2.03	3
100 steps	0.02	1.63	7
	0.05	1.99	9
	0.1	2.22	9
	0.5	2.25	7
	1	2.28	4
	2	2.23	3
50 steps	0.02	1.77	7
	0.05	2.22	9
	0.1	2.47	9
	0.5	2.55	7
	1	2.39	4
	2	2.39	4

Note: The relevant properties are $k = 1000$ and $\varepsilon = 0.01$.

and, more recently, Chen and Harker [18] have shown that it is the case under the conditions given below. The statement of the NCP is:

Find $\mathbf{x}$ in $\mathbb{R}^n$ such that $x_i \geqslant 0$, $G(x_i) \geqslant 0$ and $G(x_i)x_i = 0$. This is equivalent to $x_i = [x_i - G(x_i)]_+$

where $\mathbf{G}(\mathbf{x})$ is a differentiable function from $\mathbb{R}^n$ to $\mathbb{R}^n$. Note that, due to non-negativity of the components, it follows that $G(x_i)x_i = 0 \Leftrightarrow \mathbf{x} \cdot \mathbf{G}(\mathbf{x}) = 0$.

An NCP is said to be strongly monotone if

$$\exists k \in \mathbb{R}^+ : \forall \mathbf{x}, \mathbf{y} \in \mathbb{R}^n \quad [\mathbf{G}(\mathbf{x}) - \mathbf{G}(\mathbf{y})] \cdot (\mathbf{x} - \mathbf{y}) \geqslant k \|\mathbf{x} - \mathbf{y}\|^2$$

It is known that a strongly monotone NCP has a unique solution (see [18]).

For a Lipschitz continuous $G(\mathbf{x})$ (i.e. $\exists K \in \mathbb{R} : \|G(\mathbf{x}) - G(\mathbf{y})\| \leqslant K \|\mathbf{x} - \mathbf{y}\|, \forall \mathbf{x}, \mathbf{y} \in \mathbb{R}^n$) and strongly monotone NCP, let $\mathbf{x}(\alpha)$ be a solution of $x_i - p[x_i - G(x_i), \alpha] = 0$, $i = 1, \ldots, n$. Then, for the solution $\bar{\mathbf{x}}$ of the NCP it follows that

$$\exists C_p \in \mathbb{R}_+ : \quad \|\mathbf{x}(\alpha) - \bar{\mathbf{x}}\|_p \leqslant C_p \gamma_p \log(2)/\alpha, \quad p = 1, 2, \infty \tag{9}$$

with $\gamma_1 = n, \gamma_2 = \sqrt{n}$ and $\gamma_\infty = 1$. The existence of a solution for the smoothed problem ($\mathbf{x}(\alpha)$) is still subject to proof under the previous conditions. For a solvable NCP, the theorem (the proof is given by Chen and Mangasarian [17]) is as follows.
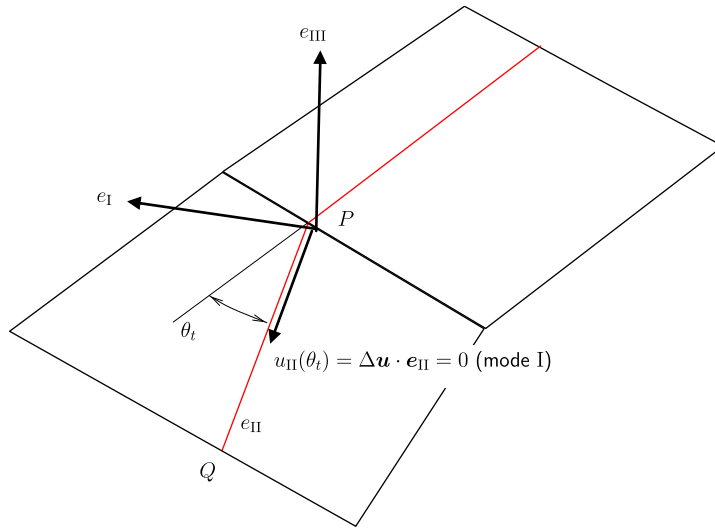
Figure 7. An example for mode I crack orientation based on zero stress jump.

Theorem 1
Let the NCP be solvable. If $\delta_1 \geqslant \log 2$ and $\alpha > 0$, the NCP conditions are approximately satisfied as

$$(-x)_+ \leqslant \frac{\delta_1}{\alpha} \mathbf{1}, \quad (-\mathbf{G}(\mathbf{x}))_+ \leqslant \frac{\delta_1}{\alpha} \mathbf{1}, \quad [\mathbf{x} \cdot \mathbf{G}(\mathbf{x})]_+ \leqslant \frac{nC(\delta_1)}{\alpha^2}$$

$$\text{with } C(\delta_1) = \max\{2, (e^{\delta_1} - 1) \log^2(e^{\delta_1} - 1)\}$$

For the present applications, it remains to show that our NCP is strongly monotone. Even for Hookean elasticity, this condition cannot presently be ensured. For a LCP, Tin-Loi and Tseng [31] also mention this problem, but the application of the solution method does not appear to be affected.

3.3. Treatment of a prototype cohesive law

The set-valued cohesive law shown in Figure 3 can be given by the following non-smooth equation:

$$\text{eq}(d, f) = 0 \tag{10}$$

A corresponding smoothed version for the non-degenerate case is introduced by making use of the smoothing parameter $\alpha(\text{tol})$ in (6):

$$\text{eq}_s[d, f, \alpha] = \text{eq}_1[d, f, \alpha] ab + \text{eq}_2[d, f, \alpha](1 - ab) \tag{11}$$

with

$$\begin{aligned}
a &= s(\widetilde{d} - d, \alpha) \\
b &= s\left(d_c - d_c \frac{f}{f_{\max}}, \alpha\right)
\end{aligned} \tag{12}$$
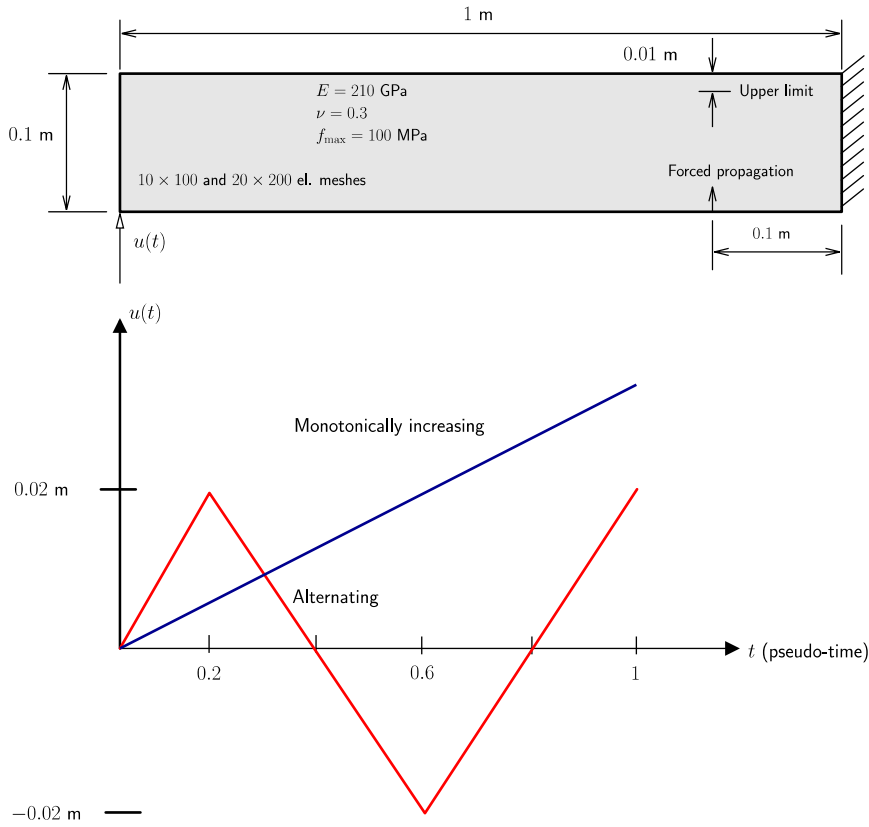
Figure 8. Beam bending under cyclic loading. Relevant properties, boundary
conditions and geometrical data.

and

$$
\begin{aligned}
\mathrm{eq}_1[d, f, \alpha] &= d - p\left[d + \widetilde{d}\,\frac{f}{f_{\max}} - \frac{d}{d_c}(d_c - \widetilde{d}), \alpha\right] \\
\mathrm{eq}_2[d, f, \alpha] &= p[d_c - d, \alpha] - \frac{d_c f}{f_{\max}}
\end{aligned}
\tag{13}
$$

which, for $G_c = 0.5$ and $f_{\max} = 1$, is represented in Figure 4 for several values of $\widetilde{d}$ and tol.

The gradient of $\mathrm{eq}_s(d, f)$ can be calculated using the chain rule. This is performed with a computer algebra software. However, it is interesting to represent it in the space d–f for our specific material properties (see Figure 5) with tol $= 0.5$ and $\widetilde{d} = 0.2$. Note that the derivatives are also smooth, and therefore a (non-symmetric) smooth solver can be used to solve the algebraic non-linear system:

$$
\mathbf{F} = \left\{ \begin{array}{c} \mathbf{r}_{\mathrm{equ.}}(\mathbf{u}, \mathbf{f}) \\ \mathbf{eq}_s[\mathbf{d(u)}, \mathbf{f}] \end{array} \right\} = \mathbf{0}
\tag{14}
$$
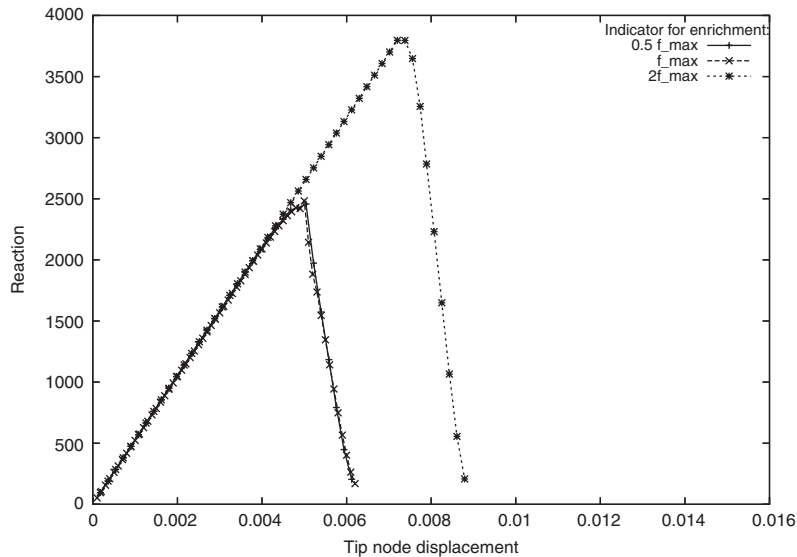
Figure 9. Effect of premature and delayed enrichment time in the load–deflection results ($G_c = 5000\,\text{N/m}$).

for **u** and **f**. In system (14), $\mathbf{r}_{\text{equ.}}$ represents the vector of discrete equilibrium equations (n components), $\mathbf{eq}_s$ represents the vector of smoothed conditions (m components). The non-linear system with $m + n$ unknowns is solved by the trust-region method shown in Table I, also see [34]. The degrees of freedom corresponding to **f** and **d** are scaled (with the conditions $f \neq f_{\text{max}}$ and $d \neq d_c$) so that the cohesive law is the one depicted here.

The non-linear solver makes use of the Jacobian of (14), which is generally non-symmetric:

$$\mathbf{K} = \begin{bmatrix} \dfrac{\partial \mathbf{r}}{\partial \mathbf{u}} & \dfrac{\partial \mathbf{r}}{\partial \mathbf{f}} \\[2ex] \dfrac{\partial \mathbf{eq}_s}{\partial \mathbf{u}} & \dfrac{\partial \mathbf{eq}_s}{\partial \mathbf{f}} \end{bmatrix} \tag{15}$$

The number of degrees of freedom and sparsity pattern of (15) change during the solution.

A characteristic which is different from previous implementations of the cohesive law in the context of XFEM is that caution should be taken to avoid duplication of constraints. Note that after exhaustion of the cohesive law ($\widetilde{d} > d_c$) the diagonal term $f - f$ of the Jacobian is equal to 1, and therefore no elimination of the corresponding f degree of freedom is required. System (14) is solved by a monolithic approach.

A simple test for the use of the trust-region method and fixed time steps is depicted in Figure 6.

Note that there are no signs of ill conditioning, but the method entails the costs of a non-symmetric Jacobian.

For $k = 1000$, we test the sensitivity of the non-linear solver with respect to the solution parameter tol and also the average number of time steps n_{step}. The monitored quantities are the average number of iterations $n_{\text{iter}}^{\text{av}}$ and the maximum number of iterations in a given step $n_{\text{iter}}^{\text{max}}$. The initial
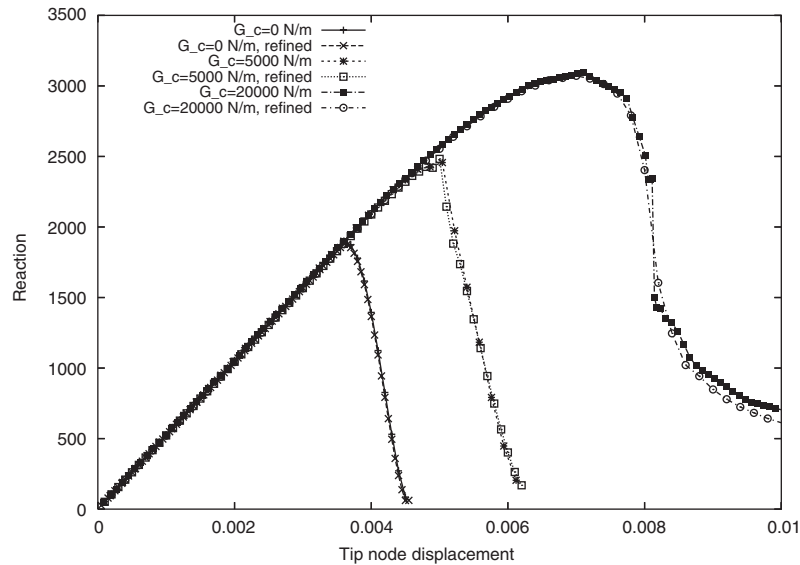
Figure 10. Beam under in-plane bending with monotonic end loading. Load–deflection results. The time steps are shown as point markings.

trust radius is 1 and a tolerance of $tol_{tr} = 1 \times 10^{-6}$ is employed for the trust-region method. Table II shows the results. A near insensitivity to the curvature is noted.

4. CRACK ADVANCE CRITERION AND ORIENTATION

For cohesive cracks, the crack advance problem is of more direct address than for non-cohesive cracks. From a strict reading of Barenblatt's work, the advance of a crack is supported by the existence of an initial positive slope (and zero stress for zero displacement) in the stress–displacement law. We already observed that this is not consistent with a continuum–discontinuum transition, as it would cause an abrupt unloading of neighbor regions.

Our theory for crack advance is based on the similarity (in loading) of the crack tip cohesive stress distribution (Barenblatt's second hypothesis and Goodier's third postulate [25]). When a new extension of the crack surface is required, we assume that, at the instant of surface creation, the new part of the cohesive stress cancels the pre-existent normal stress distribution. This is equivalent to assuming that *no stress jump occurs*. From this condition, we obtain both the orientation of newly formed crack surfaces and the crack advance. The former is calculated from the zero jump condition and the latter is obtained from the internal force required to close the tip. We introduce the condition for advance:

$$\mathbf{f}_{\text{tip}} \cdot \mathbf{e}_{\text{I}} < 0 \tag{16}$$

where $\mathbf{f}_{\text{tip}}$ is the internal force at the tip, resulting from the combined effects of opening forces and the cohesive law. In loading, a cusp-shaped tip closing is expected to correspond to a null (resulting) stress intensity factor, as discussed by Barenblatt [1]. For sufficiently long cohesive tails
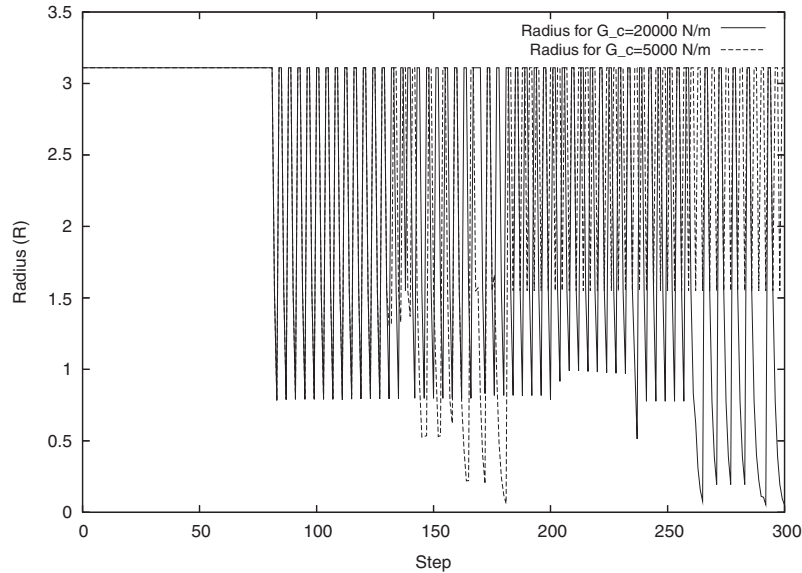
Figure 11. Beam under in-plane bending with monotonic end loading. Variation of the trust radius (R) for all iterations and time steps.

(Figure 16 shows a typical cohesive tail), the traditional finite element resolution can be adequate to represent this cusp. We verify this in plate bending numerical examples.

To obtain the orientation of a pre-existent cohesive crack, we make use of the fact that no jump in stresses should occur when the surface is formed. With a cohesive law, if we have pure mode I, this is equivalent to having zero tangential displacement, as a non-zero value would mean that a tangential stress would be released upon crack advance. The same terms can be applied for modes II and III. This criterion is of an extraordinary simplicity; an illustration is given in Figure 7. It can be directly obtained from the crack tip opening displacement components decomposed along each of the directions represented in the figure. Details about how this is performed are given by Sutton *et al.* [36] for a somehow different situation (the Erdogan–Sih criterion).

For the elasto-plastic case (not discussed here), the COD concept is still applicable, whereas the application of configurational integrals is subject to certain conditions (such as inhibition of unloading).

5. NUMERICAL EXAMPLES

Results from verification tests are presented. The examples serve to inspect the main ingredients of the method and also the implementation. In post-processing, elements are *divided* to create realistic crack evolution pictures.

Elasticity is considered (using the Saint–Venant model) and the piecewise linear cohesive model with tol $= 0.01 d_c$. For the trust-region method we use a tolerance of $\text{tol}_{\text{tr}} = 1 \times 10^{-6}$. Small enough
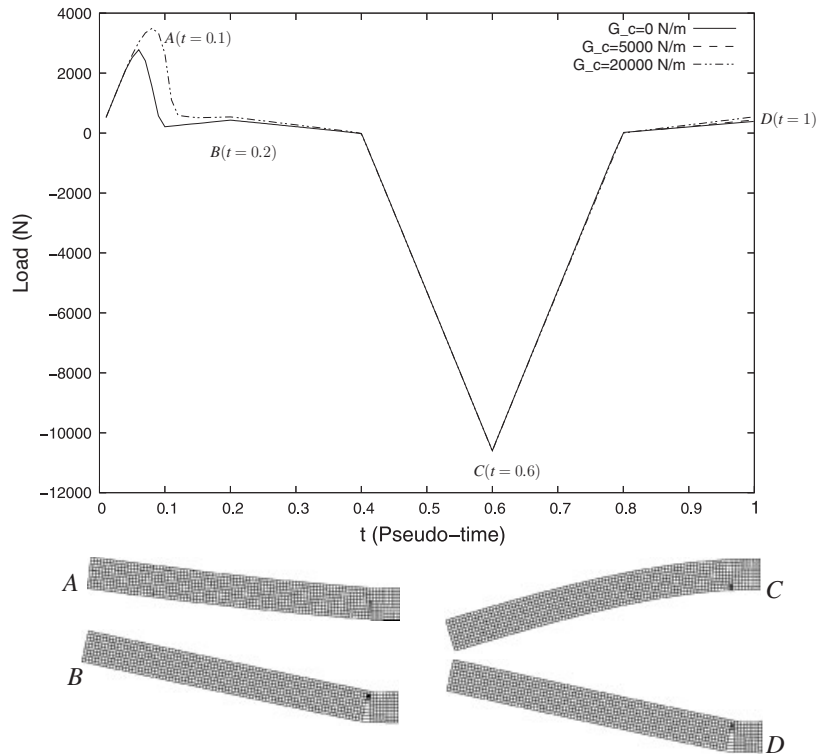
Figure 12. Beam under in-plane bending with oscillatory end loading. Load–deflection results and deformed meshes (magnified 10×). Also represented are the cohesive forces, with a maximum of 100 MPa for the tension cases and a minimum of -534 MPa for the compression case.

load (and displacement) steps are used to avoid spurious crack holding. The advance can occur for any number of elements ahead of the tip.

5.1. In-plane bending of a beam

A rectangular beam subject to in-plane loading is tested for several values of the fracture energy. The overall response and the effect of mesh refinement are inspected. This test is essentially a plane stress situation in mode I as rotations and out-of-plane motion are prescribed (the independent opening of top and bottom surfaces is performed in the subsequent example). The relevant properties are shown in Figure 8. A number of features are intentionally left out from this test, so that conclusions concerning the cohesive law can be obtained without added complications.

With a monotonic imposed displacement $u(t) = u_0 t$, the load–deflection results are shown in Figure 10 for three values of the fracture energy $G_c \in \{0, 5000, 20\,000\}$ N/m. For verification purposes, in this example the Rankine criterion is adopted. The evolution of the radius of the trust-region method is depicted in Figure 11 for the cases $G_c = 5000$ N/m ($d_c = 0.1$ mm) and $G_c = 20\,000$ N/m ($d_c = 0.4$ mm). The radius value is reset every time step. Clearly, we can see why classical Newton implementations (even with line search) are inefficient for NCP and LCP
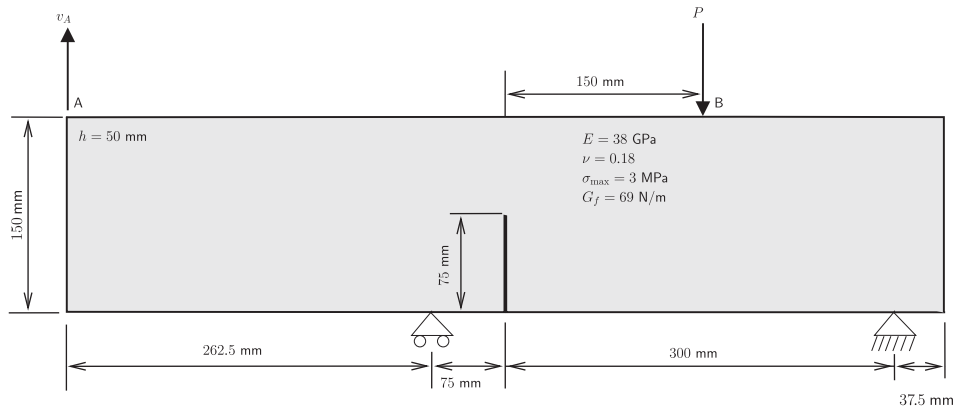
Figure 13. Relevant data for the single-edge notched beam (see details in Reference [37]).
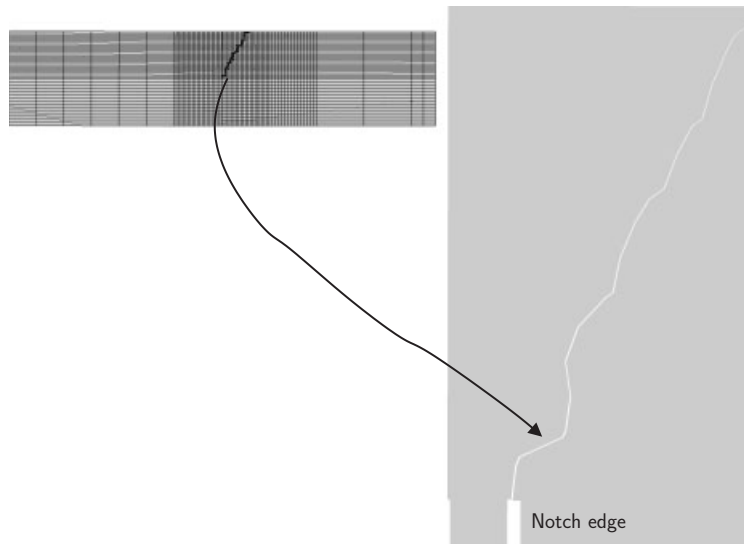The mesh contains 2625 elements.

Figure 14. Crack path (over the real deformed geometry) and tip detail for the single-edge notched beam.

(such as elasto-plasticity). The combination of Cauchy step with the Newton step allows a robust solution without step cuts. Note that small steps are used to ensure accuracy in the integration. Any step size can be used, and the method never failed to converge during our test session, but some preliminary convergence study is advised.

Another revealing test can be performed by starting the enrichment before the stress reaches f_{max}. The points in the $d-f$ diagram should be in the vertical loading region $d=0$, $f \leqslant f_{max}$ and therefore the results should not be affected by the early enrichment. The same cannot be said about delayed enrichment. For the finer mesh and $G_c = 5000 \, \text{N/m}$ this fact is illustrated in Figure 9.
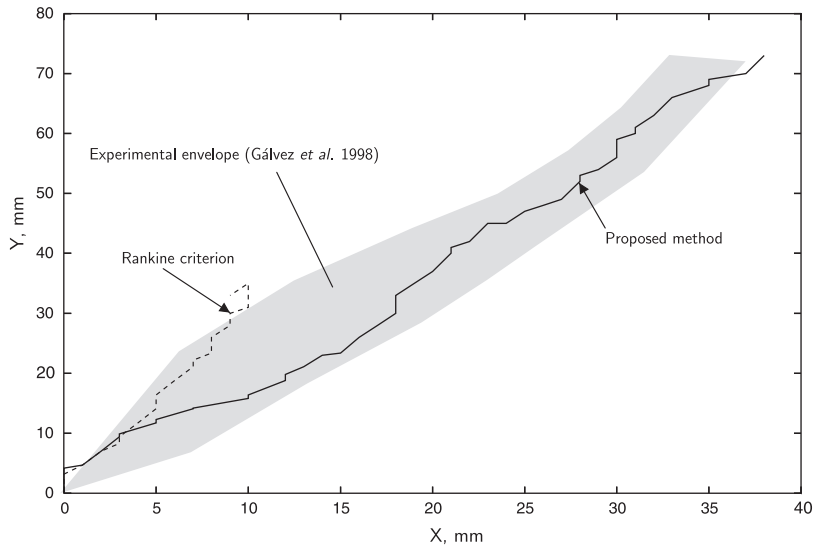
Figure 15. Crack path comparison between the proposed method and the Rankine criterion for the single-edge notched beam.
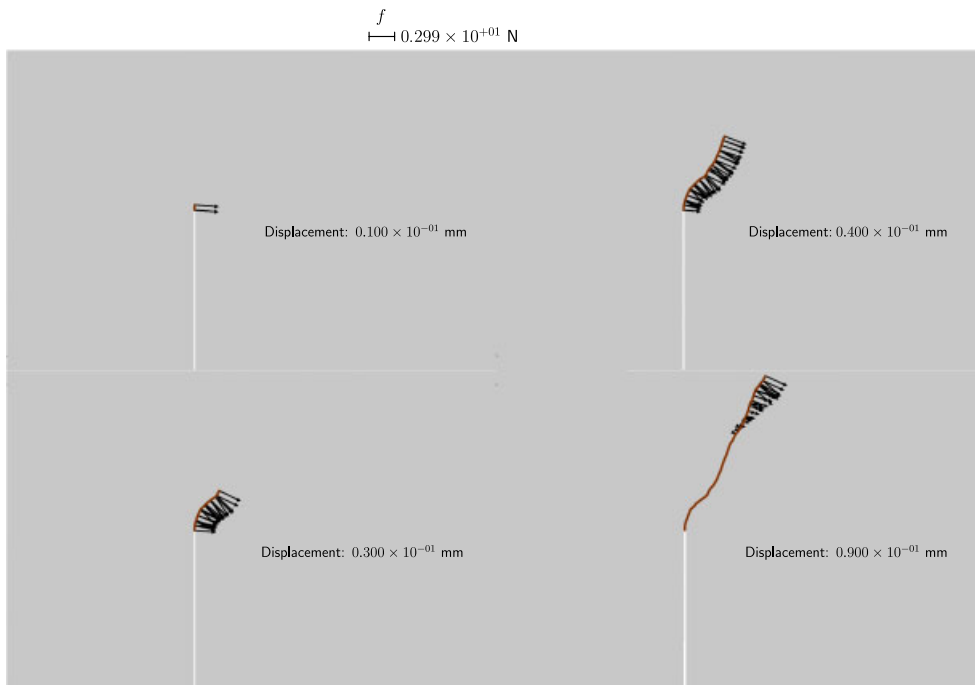

Figure 16. Sequence of time steps with the distribution of the cohesive stress f. The value of the vertical displacement of point B in Figure 13 is shown. Note that only the relevant propagation region is depicted.
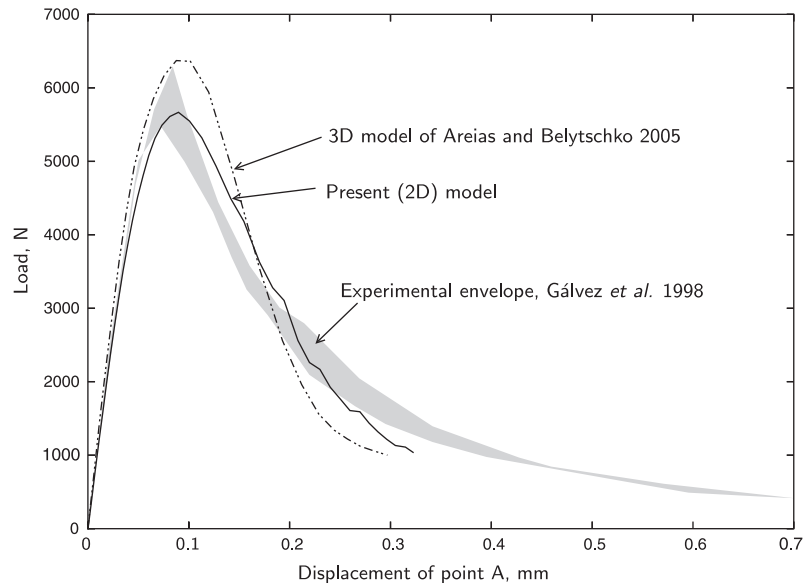
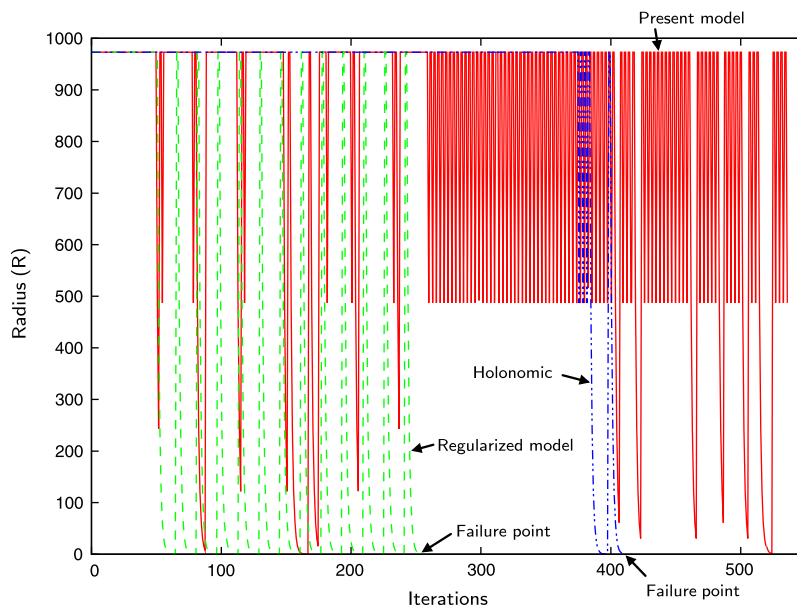Figure 17. Single-edge notched beam: load *versus* displacement of point A, v_A. The experimental envelope from [37] is also shown.

Figure 18. Single-edge notched beam: trust radius as a function of the number of iterations for all time steps. For comparison, the results of a regularized model (with a penalty parameter equal to $f_{\max} 1 \times 10^3 / d_c$) are also shown, along with the holonomic case.
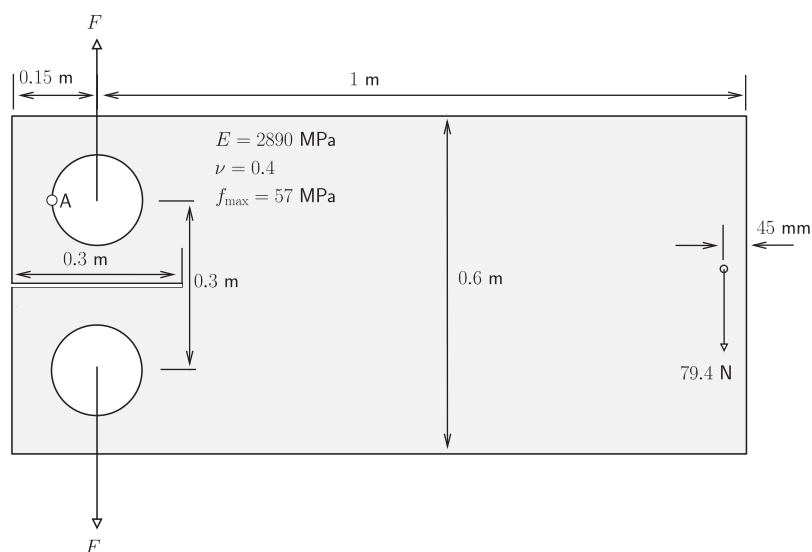
Figure 19. Geometry, boundary conditions and relevant material properties for
the double-edge notched beam.

We can see that premature enrichment is not critical (for proportional loading), confirming the correct implementation of the degenerate situation shown in Figure 3. The two classical methods to introduce a cohesive law (either holonomic or regularized) are obviously unable to provide this type of immunity to premature enrichment.

For higher values of the critical energy release rate, a decrease of the stress at the tip is observable when premature enrichment is forced.

For an imposed end displacement of the piecewise linear type, the load–deflection results are shown in Figure 12. The (averaged) stress forces f at the elements containing a crack for the case $G_c = 20\,000\,\text{N/m}$ with a $10\times$ magnification are also shown. We can observe the damage effect resulting from the cohesive law: the compliance is substantially increased after application of one load-reversal cycle. Another result to retain is that a very sharp curve is obtained in the reversals, which corroborates our indication that the problem is being correctly solved. No artificial detachments or spurious responses occurred. During the compression stage, it was noted that the cohesive force was zero in some points and hence some detachment should occur.

5.2. Verification of the crack path and the cohesive stress

An inspection of the 2D crack path obtained with the proposed method is done using two known examples from the literature. The first example is a plain concrete fracture test [37] of a notched plate asymmetrically loaded by a vertical point load.

The problem is summarized in Figure 13. The cracked beam and the tip detail are shown in Figure 14. A comparison between the Rankine criterion (without averaging) and our model is presented in Figure 15, along with the envelope of experimental results reproduced from [37]. In addition to the manifest good behavior in this linear-elastic problem, our criterion is not conditioned by the underlying constitutive model. In the implementation, the criterion is applied directly in the
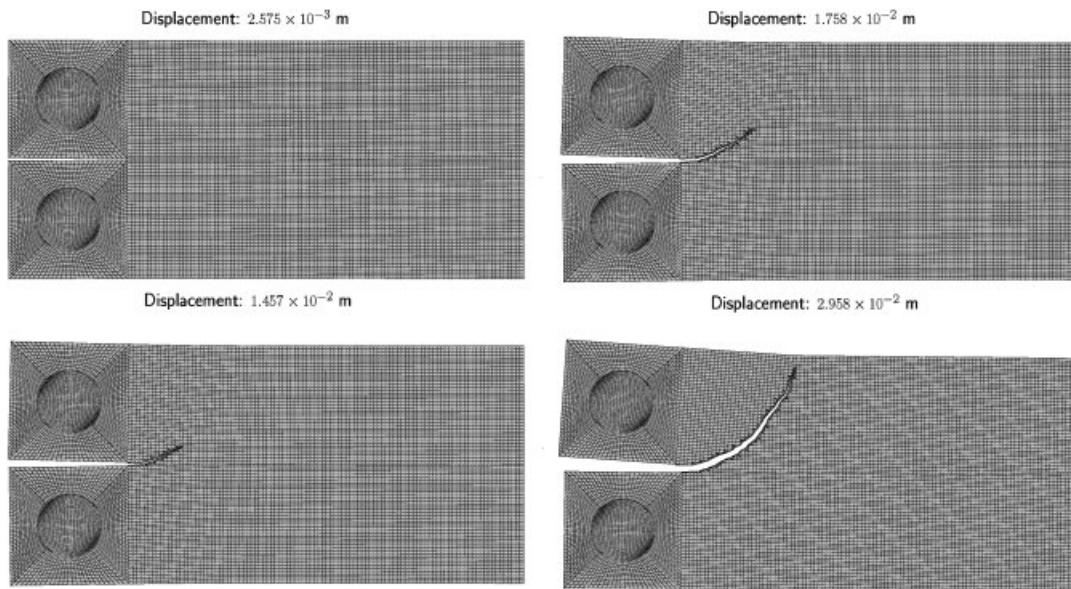
Figure 20. Sequence of deformed (coarse) meshes with explicit crack path.
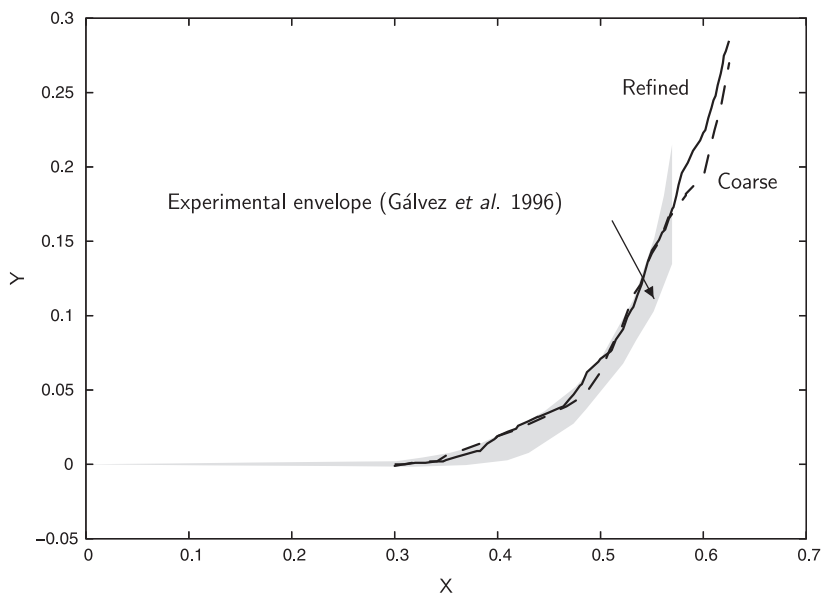The displacement of point *A* is monitored.

Figure 21. Experimental [39] and predicted crack paths. The coarse mesh contains 12 700
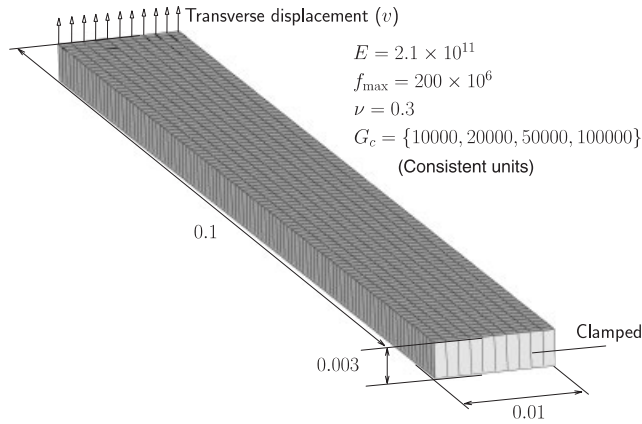elements and the refined mesh 40 400.

Figure 22. Out-of-plane bending of a beam: mesh, boundary conditions and material properties (discretization with 1000 elements). Consistent units are used.
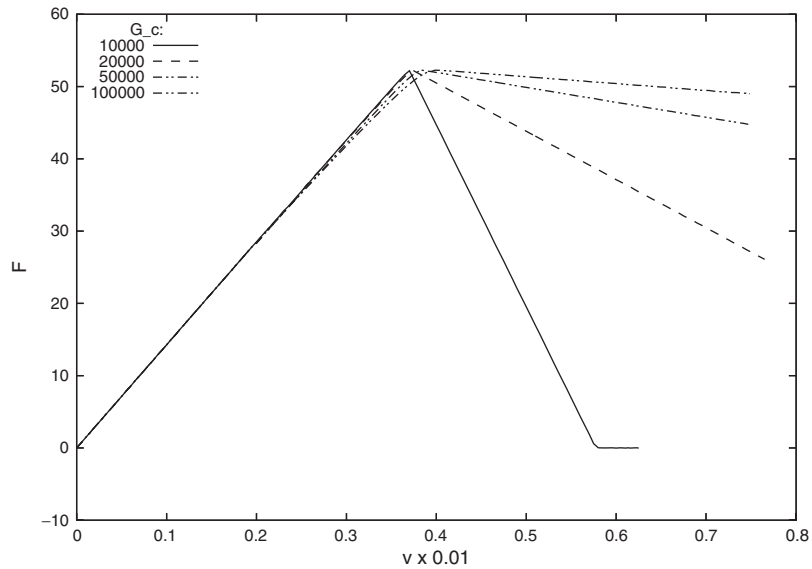

Figure 23. Load–deflection results for several values of G_c.

first intersection of the crack core with an element edge. The distribution of the cohesive force f is given for a sequence of time steps in Figure 16.

The irregularity noted with the Rankine-calculated path is caused by the incompatible stress field. An inversion of the crack path trajectory occurs and the analysis stops prematurely. This result of the Rankine criterion is not unforeseen.

The load–deflection curve is given in Figure 17, along with the experimental envelope and the results from Areias and Belytschko [38] who used a 3D model with regularized unloading. Note that averaging was used before by these authors to avoid the inversion of the crack path.
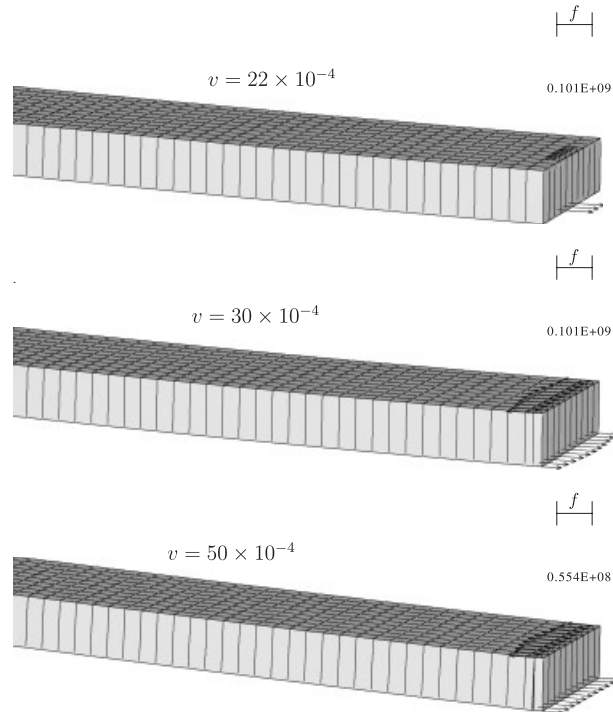
Figure 24. Evolution of cohesive stress vectors for $G_c = 10\,000$ consistent units.

A difficulty with averaging (this also applies to the domain integral) is the definition of domain size.

As the cohesive stress is an independent field, there is a complete decoupling with the continuum. In terms of root-finding convergence, the resulting properties are exceptionally good, as can be observed in Figure 18. Usually one iteration is performed in each time step. The trust radius only reduces when closing/opening iterations occur. For comparison, a regularized cohesive law and the holonomic case are also shown. It is clear that, if we exclude unloading, the problem is almost linear and the convergence behavior is very good before the discontinuous transition. When this is reached, the method fails to converge. In addition, although use can be made of the original Barenblatt condition in closed form (see the seminal work of Moës and Belytschko [26]), the model is incomplete. The regularized model also fails to converge prematurely, as shown in that figure.

The second example is a double-edge notched beam subject to two opposing opening forces and a third constant force in the right edge. This third force induces a smooth crack turning away from the notch orientation.

This example was initially proposed by Gálvez *et al*. [39] as a test for the accuracy of numerical implementations of crack growth. In that paper, the Erdogan–Sih criterion (see [33]) was used with success. As shown by Shen and Shen [40], this criterion coincides with the minimization of the potential energy with respect to the kink angle, for elastic isotropic materials.
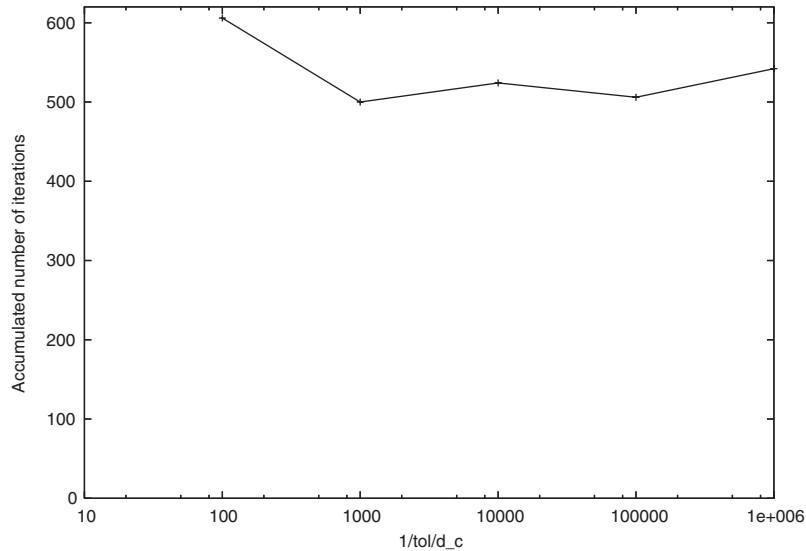
Figure 25. Results (tol/d_c) *versus* number of iterations ($n_{\text{iter}}^{\max}$) for $G_c = 10\,000$ and $v = 6.25 \times 10^{-3}$.

However, it requires the values of the stress intensity factors (they can be calculated with a variety of techniques, such as the J-integral or extracted from the COD components) and also specialized tip elements. The present method, besides being applicable to general non-linear situations, can be used with standard element formulations.

Figure 19 shows the relevant ingredients of the problem. The deformed mesh with a crack is shown in Figure 20. The crack path under proportional loading obtained with our method is clearly smooth (Figure 21).

A comparison with the experimental envelope of Gálvez *et al*. [39] is shown in Figure 21. There is a good agreement between the experimental data and the predicted results. Note that the fracture of PMMA requires large strain capabilities.

5.3. Out-of-plane bending

It can be observed that less intricate methods are available to obtain some of the previous results. In the presence of out-of-plane bending, the method works differently.

In rods, plates and shells, through-the-thickness cracks occur when at least one, but not necessarily all, point in a given cross-section satisfies a critical condition. If not critical, the remaining points should then behave as if no crack existed.

Let us consider the beam depicted in Figure 22. Load–deflection results for this new situation are shown in Figure 23. For $G_c = 10\,000$, the evolution of the cohesive stress vectors at the boundary is shown in Figure 24. It can be seen that a non-uniform distribution of stress magnitudes occurs in compression. For $v = 22.0 \times 10^{-4}$ only the inner core of the clamped region is cracked. The lower edge of the clamped region is under tension and opening whereas the upper region closes in contact and adhesion because $f < f_{\max}$. It can be observed that shell kinematics are sufficient to model a wide variety of crack propagation situations.
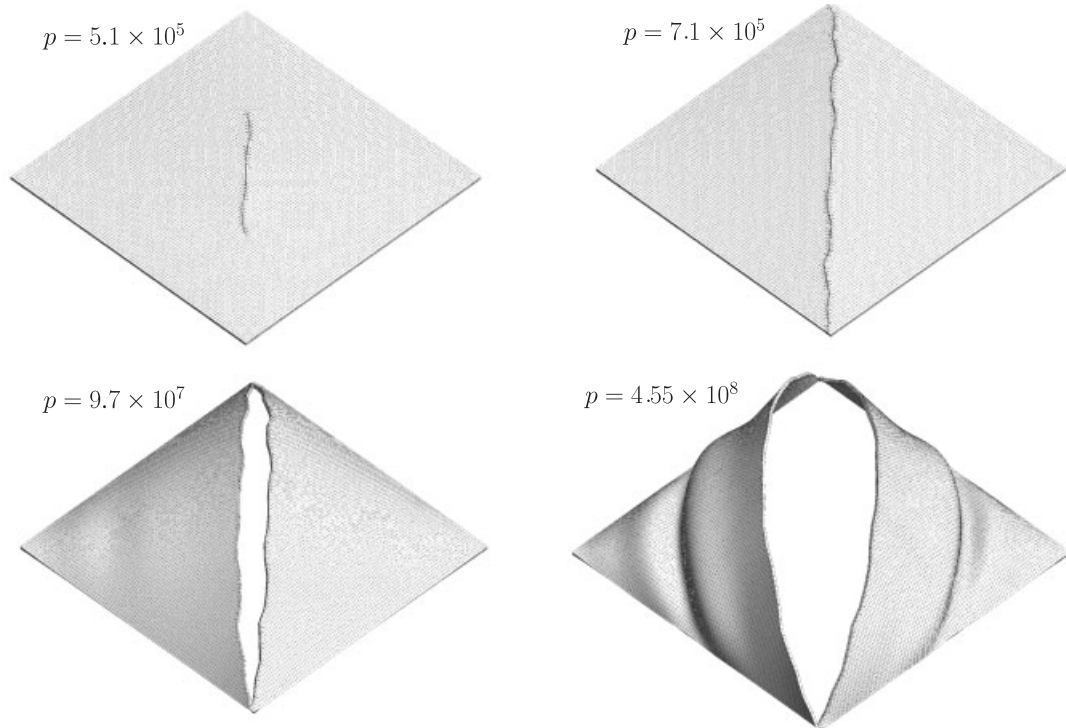
Figure 26. Square plate under pressure: sequence of deformed configurations (non-prescribed crack path). The refined mesh is shown.

To inspect the solution performance, a tolerance (tol) *versus* number of iterations ($n_{\text{iter}}^{\max}$) study is performed for $G_c = 10\,000$ and using the last analysis point shown in Figure 25 (it corresponds to $v = 6.25 \times 10^{-3}$). We choose this case as it forces the crossing of two high curvature regions in loading. The relative DOF tolerance is $\text{tol}_{\text{tr}} = 1 \times 10^{-7}$. Figure 25 shows that the total number of iterations is nearly independent of tol. Therefore, the smoothed law can be made as accurate as desired.

5.4. Crack path in a simply supported square plate

This example shows mode I fracture in a simply supported square plate subject to uniform, motion-dependent pressure. The purpose here is to test the crack path algorithm in mode I. The plate dimensions are $1 \times 1 \times 0.01$ consistent units, the elastic properties are $E = 210 \times 10^9$, $v = 0.3$ for the elasticity modulus and the Poisson coefficient, respectively. The maximum normal stress is $f_{\max} = 500 \times 10^6$. The crack path is calculated using the COD. Two regular meshes are used: 20×20 and 100×100.

A sequence of deformed configurations is shown in Figure 26. The displacement components of the mid-surface are prescribed at the boundary and therefore pressure can increase up to very high values. Owing to the use of COD components, the determination of the crack path requires an element-by-element approach, and this results in some irregularity, also seen before in the 2D example. In reality, inhomogeneity will eventually produce an analogous effect. We inhibited the
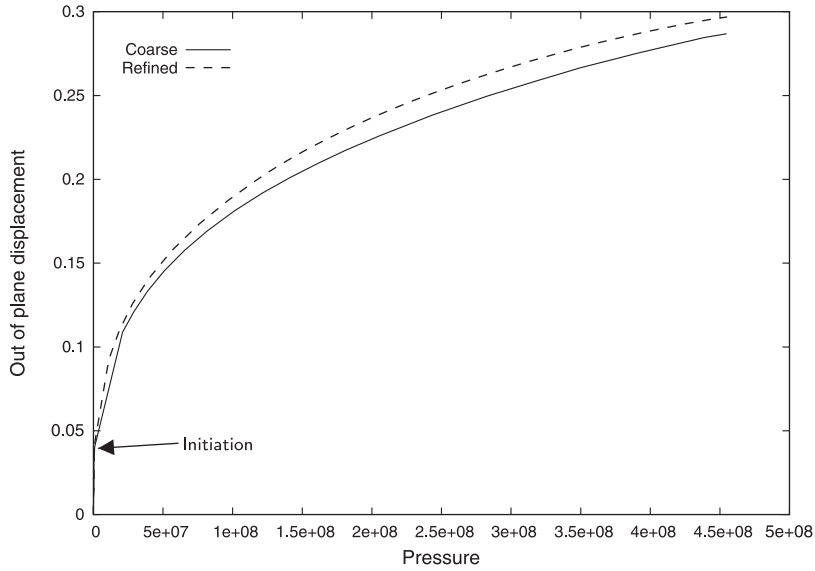
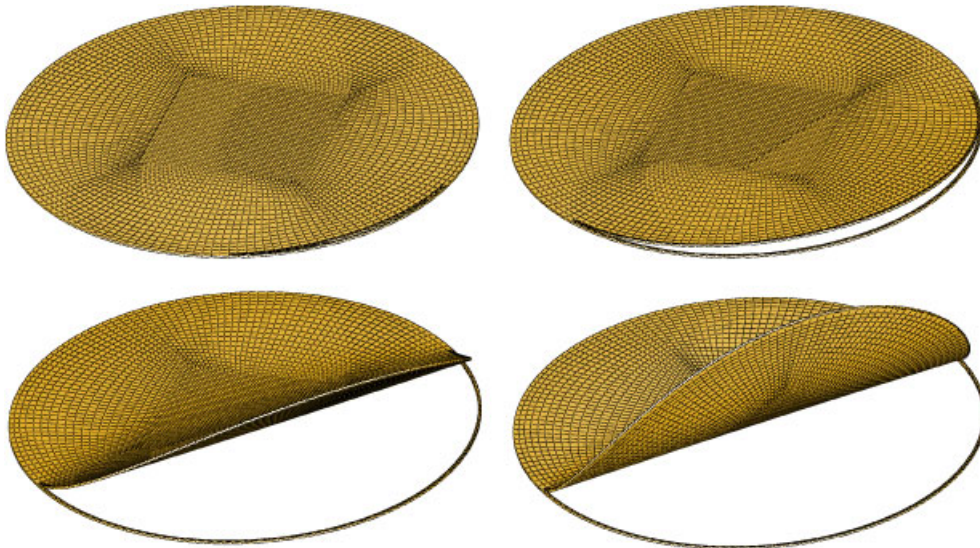Figure 27. Square plate: pressure/mid-point displacement results.

Figure 28. Circular plate under uniform pressure: sequence of time steps.

'crossed' crack pattern known to occur in the simply supported case, as this would create an unnecessarily complex situation for the degrees of freedom in the center of the plate (usually this is solved empirically by removing the affected element). Wrinkles occur around the main crack because pressure starts to bend the crack faces.

$p = 20000$

f

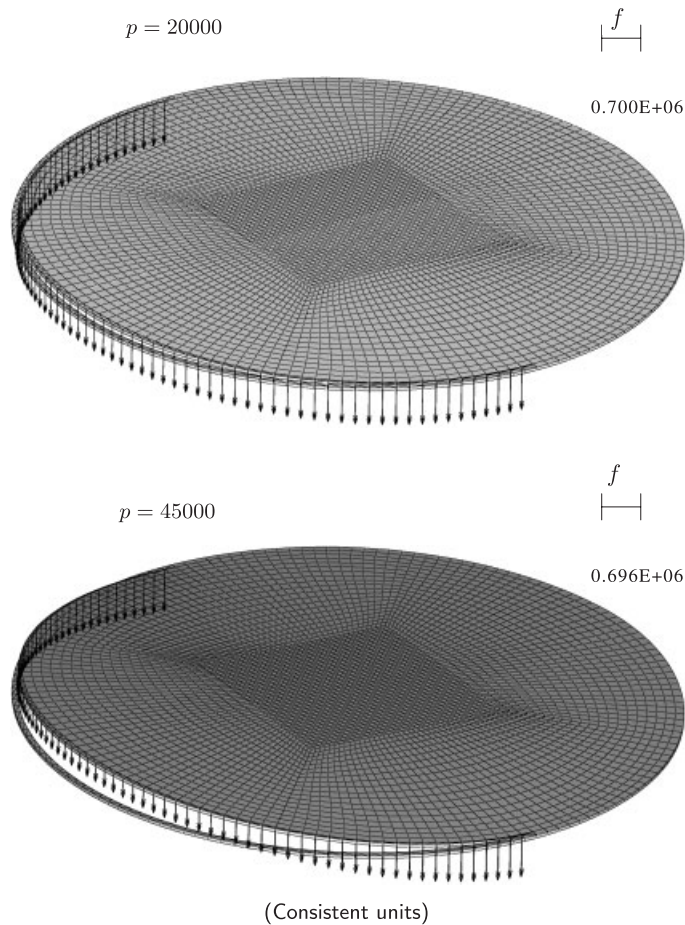0.700E+06

$p = 45000$

f

0.696E+06

(Consistent units)

Figure 29. Circular plate under uniform pressure: cohesive stress vectors.

The pressure *versus* mid-point displacement results are shown in Figure 27 for the coarse and refined meshes. Some difference is observable, since crack paths are slightly distinct. In addition, localized bending behavior tends to increase the out-of-plane displacement at the plate's center.

5.5. Circular plate under pressure: mode III

A clamped circular plate with uniform mid-surface pressure is allowed to fracture in a circular section of the clamped boundary. Consistent units are used; the plate radius is 1 and thickness is 0.01. The elasticity modulus is $E = 210 \times 10^9$, the Poisson coefficient is $v = 0.3$ and the maximum shear stress is $f_{\max} = 7 \times 10^5$. The maximum applied pressure is $p = 1 \times 10^6$.

A small premature crack originating from an imperfection (90% of the critical stress) is triggered in two elements in that region.

Three mesh densities (1200, 2700 and 4800 elements) and two values of fracture energy ($G_c = 0$ and $G_c = 50000\,\text{N/m}$) are used for comparison. A critical value of 2 degrees in the CTOA is
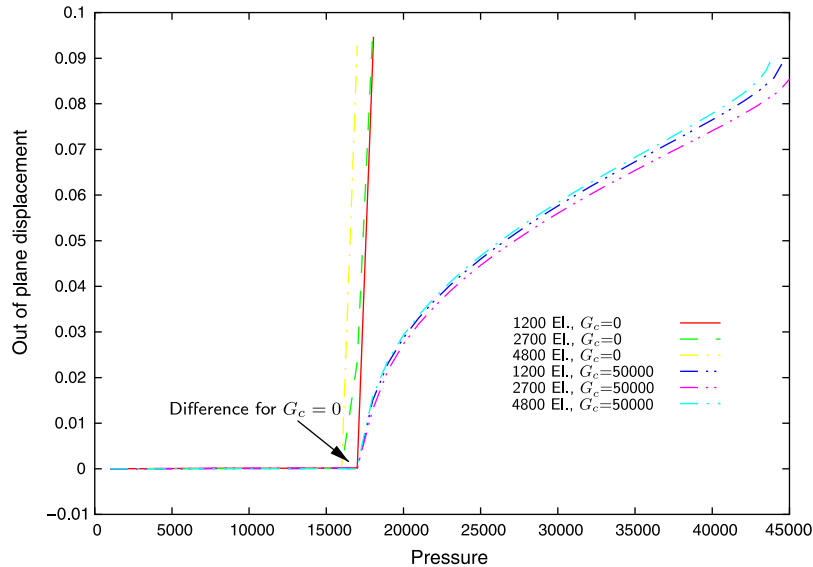
Figure 30. Circular plate under uniform pressure: load *versus* out-of-plane displacement.

employed for the crack advance in the $G_c = 0$ case. Pressure is increased in steps of 500 consistent units which were found to be sufficient to avoid artificial crack arrest.

A sequence of deformed meshes with the cohesive vectors is shown in Figure 28. The evolution of the cohesive stress vectors (the product of mode III direction and the force degree of freedom) at early stages is represented in Figure 29. Relatively large openings still produce substantial stress.

The load *versus* out-of-plane displacement results are shown in Figure 30. Robust and reasonably mesh-independent results are obtained. It is worth noting that the fracture indicator has a substantial effect if $G_c = 0$. A difference in the pressure value is indicated in Figure 30. The reason for this is that cohesive forces are absent and therefore a sudden jump occurs at initiation. If $G_c \neq 0$, there is no difference, since the cohesive forces hold the two parts together before the release. The difference can be eliminated by using a small value for G_c.

6. CONCLUSION

The equilibrium problem with a cohesive traction-separation law was written as a complementarity problem. A method based on smooth replacement of the plus and sign functions involved in the complementarity problem was introduced. This allowed a classical root-finding method to be applied to an enlarged algebraic non-linear (and non-symmetric) system, but involving smooth functions only. Specifically, a variant of the trust-region method was used in the solution of this problem.

Within this framework, loading, reloading and unloading situations were represented as accurately as desired. The method allowed the use of through-the-thickness cracks in plates for situations where not all the points along the thickness were critical at initiation. It was also verified that the

crack path could be directly determined, and the method was applied to a variety of situations with a high degree of success. The fracture propagation part of the code is now very robust.

REFERENCES

1. Barenblatt GI. The mathematical theory of equilibrium of cracks in brittle fracture. *Advances in Applied Mechanics* 1962; **7**:55–129.
2. Planas J, Elices M. Nonlinear fracture of cohesive materials. *International Journal of Fracture* 1991; **51**:139–157.
3. Bažant ZP, Planas J. *Fracture and Size Effect in Concrete and Other Quasibrittle Materials*. CRC Press: Boca Raton, FL, 1998.
4. Elices M, Guinea GV, Gómez J, Planas J. The cohesive zone model: advantages, limitations and challenges. *Engineering Fracture Mechanics* 2002; **69**:137–163.
5. Planas J, Elices M, Guinea GV, Gómez FJ, Cendón DA, Arbilla I. Generalizations and specializations of cohesive crack models. *Engineering Fracture Mechanics* 1996; **70**:1759–1776.
6. Alfano G, Crisfield MA. Finite element interface models for the delamination analysis of laminated composites: mechanical and computational issues. *International Journal for Numerical Methods in Engineering* 2001; **50**: 1701–1736.
7. Kubair DV, Geubelle PH. Comparative analysis of extrinsic and intrinsic cohesive models of dynamic fracture. *International Journal of Solids and Structures* 2003; **40**:3853–3868.
8. Sam C-H, Papoulia KD, Vavasis SA. Obtaining initially rigid cohesive finite element models that are temporally convergent. *Engineering Fracture Mechanics* 2005; **72**:2247–2267.
9. Papoulia KD, Sam C-H, Vavasis SA. Time continuity in cohesive finite element modeling. *International Journal for Numerical Methods in Engineering* 2003; **58**:679–701.
10. Leine RI, Nijmeijer H. *Dynamics and Bifurcations of Non-smooth Mechanical Systems*. Springer: Berlin, 2004.
11. Bolzon G, Maier G, Tin-Loi F. On multiplicity of solutions in quasi-brittle fracture computations. *Computational Mechanics* 1997; **19**:511–516.
12. Belytschko T. Private communication, 2003.
13. Huespe AE, Oliver J, Pulido MDG, Blanco S, Linero D. On the fracture models determined by the continuum-strong discontinuity approach. *International Journal of Fracture* 2006; **137**:211–229.
14. Areias PMA, César de Sá JMA, Conceição António CA, Carneiro JASAO, Teixeira VMP. Strong displacement discontinuities and Lagrange multipliers in the analysis of finite displacement fracture problems. *Computational Mechanics* 2004; **35**:54–71.
15. Areias PMA, Song JH, Belytschko T. Analysis of fracture in thin shells by overlapping paired elements. *Computer Methods in Applied Mechanics and Engineering* 2006; **195**(41–43):5343–5360.
16. Pang J-S. Newton's method for B-differentiable equations. *Mathematics of Operations Research* 1990; **15**:311–341.
17. Chen C, Mangasarian OL. A class of smoothing functions for nonlinear and mixed complementarity problems. *Computational Optimization and Applications* 1996; **5**:97–138.
18. Chen B, Harker PT. Smooth approximations to nonlinear complementarity problems. *SIAM Journal on Optimization* 1997; **7**(2):403–420.
19. Areias PMA, Song JH, Belytschko T. Finite-strain quadrilateral shell element based on discrete Kirchhoff–Love constraints. *International Journal for Numerical Methods in Engineering* 2005; **64**(9):1166–1206.
20. Moës N, Dolbow J, Belytschko T. A finite element method for crack growth without remeshing. *International Journal for Numerical Methods in Engineering* 1999; **46**:131–150.
21. Belytschko T, Black T. Elastic crack growth in finite elements with minimal remeshing. *International Journal for Numerical Methods in Engineering* 1999; **45**:601–620.
22. Belytschko T, Moës N, Usui S, Parimi C. Arbitrary discontinuities in finite elements. *International Journal for Numerical Methods in Engineering* 2001; **50**:993–1013.
23. Barenblatt GI. On some problems of the theory of elasticity arising in investigating the mechanism of hydraulic fracture of an oil-bearing stratum. *Prikladnaya Matematika i Mekhanika* 1956; **20**:475–486 (in Russian).

24. Barenblatt GI. On the equilibrium cracks due to brittle fracture. *Doklady AN SSSR* 1959; **127**:47–50 (in Russian).
25. Goodier JN. *Mathematical Theory of Equilibrium Cracks*, *Volume II of Fracture*, Chapter I. Academic Press: New York, 1969; 1–66.
26. Moës N, Belytschko T. Extended finite element method for cohesive crack growth. *Engineering Fracture Mechanics* 2002; **69**:813–833.
27. Eterovic AL, Bathe KJ. On the treatment of inequality constraints arising from contact conditions in finite element analysis. *Computers and Structures* 1991; **40**(2):203–209.
28. Xu X-P, Needleman A. Numerical simulations of fast crack growth in brittle solids. *Journal of the Mechanics and Physics of Solids* 1994; **42**(9):1397–1434.
29. Falk ML, Needleman A, Rice JR. A critical evaluation of dynamic fracture simulations using cohesive surfaces. *Journal de Physique IV* 2001; **11**:43–52.
30. Lanczos C. *The Variational Principles of Mechanics* (4th edn). Dover: New York, 1986. Reprint from University of Toronto Press, 1970.
31. Tin-Loi F, Tseng P. Efficient computation of multiple solutions in quasibrittle fracture analysis. *Computer Methods in Applied Mechanics and Engineering* 2003; **192**:1377–1388.
32. Tin-Loi F, Que NS. Nonlinear programming approaches for an inverse problem in quasibrittle fracture. *International Journal of Mechanical Sciences* 2002; **44**:843–858.
33. Kanninen MF, Popelar CH. *Advanced Fracture Mechanics*. The Oxford Engineering Science Series. Oxford University Press: Oxford, 1985.
34. Walmag JMB, Delhez EJM. A note on trust-region radius update. *SIAM Journal on Optimization* 2005; **16**(2): 548–562.
35. Chen B, Harker PT. A non-interior-point continuation method for linear complementarity problems. *SIAM Journal on Matrix Analysis and Applications* 1993; **14**:1168–1190.
36. Sutton MA, Deng X, Ma F, Newman Jr JC, James M. Development and application of a crack tip opening displacement-based mixed mode fracture criterion. *International Journal of Solids and Structures* 2000; **37**: 3591–3618.
37. Gálvez JC, Elices M, Guinea GV, Planas J. Mixed mode fracture of concrete under proportional and nonproportional loading. *International Journal of Fracture* 1998; **94**:267–284.
38. Areias PMA, Belytschko T. Analysis of three-dimensional crack initiation and propagation using the extended finite element method. *International Journal for Numerical Methods in Engineering* 2005; **63**:760–788.
39. Gálvez J, Elices M, Guinea GV, Planas J. Crack trajectories under mixed mode and non-proportional loading. *International Journal of Fracture* 1996; **81**:171–193.
40. Shen M, Shen M-HH. Direction of crack extension under general loading. *International Journal of Fracture* 1995; **70**:51–58.